Research Square

Preprints are preliminary reports that have not undergone peer review.
They should not be considered conclusive, used to inform clinical practice,
or referenced by the media as validated information.

Healing-phase architecture governs cryogenic damage tolerance and mechanical recovery in EMAA-modified self-healing carbon fibre/epoxy composites

Yingwei Hou
Queen Mary University of London
Leping Wu
Graphene Innovations Manchester Limited
Huanming Chen
Queen Mary University of London
Lewis Barker
Graphene Innovations Manchester Limited
Tao Liu
Tao.Liu@qmul.ac.uk

Queen Mary University of London

Research Article

Keywords: Carbon fibre composites, Self-healing, Cryogenic, EMAA, Interleaving, Spray coating, Damage tolerance

Posted Date: September 11th, 2026

DOI: https://doi.org/10.21203/rs.3.rs-10255502/v1

License: This work is licensed under a Creative Commons Attribution 4.0 International License.
Read Full License

Additional Declarations: No competing interests reported.

Healing-phase architecture governs cryogenic damage tolerance and mechanical recovery in EMAA-modified self-healing carbon fibre/epoxy composites

Yingwei Hou[a], Leping Wu[b], Huanming Chen[a], Lewis Barker[b], Tao Liu[a*]

[a]School of Engineering and Materials Science, Queen Mary University of London, E1 4NS, UK

[b] Graphene Innovations Manchester Limited, M32 0JT, UK

Corresponding author: Tao Liu (Tao.Liu@qmul.ac.uk)

Abstract

Matrix microcracking and interlaminar damage limit the use of carbon fibre/epoxy laminates in cryogenic hydrogen-storage structures, particularly where repeated thermal-mechanical cycling can generate connected damage paths. This study compares two architectures for incorporating an ethylene-methacrylic acid (EMAA) thermoplastic healing phase into carbon fibre/epoxy laminates: a continuous mid-plane interleaf and a fibre-surface spray-coated particulate phase. The influence of healing-phase placement on morphology, monotonic tensile response, cyclic stiffness retention, and residual tensile performance was evaluated at room temperature and under liquid-nitrogen immersion. Cross-sectional morphology confirmed that interleaving produced a localised EMAA-rich mid-plane region, whereas spray coating generated a distributed particulate morphology on the carbon-fibre surface. EMAA incorporation reduced room-temperature stiffness and strength owing to the lower fibre fraction and the compliant thermoplastic phase. Under cryogenic loading, all specimens stiffened markedly, and the spray-coated specimens reached a tensile strength of 166.3 MPa, comparable to the pristine specimens. During repeated loading-healing cycles, both EMAA-modified sample retained stiffness more effectively than the pristine sample. At room temperature, the interleaved and spray-coated specimens retained 88.3 ± 6.4% and 70.7 ± 8.7% of their initial modulus, respectively, compared with 51.1 ± 1.8% for the pristine specimens. Under cryogenic conditions, the interleaved specimens showed the highest residual performance, reaching an apparent strength retention of 112.7% and a 148.5% increase in final failure strain relative to the cycled pristine specimens. These results demonstrate healing-phase architecture strongly governs cryogenic damage tolerance, with mid-plane interleaving providing pronounced effective residual mechanical recovery and potential for permeability recovery through thermally activated crack closure.

Keywords

Carbon fibre composites; Self-healing; Cryogenic; EMAA; Interleaving; Spray coating; Damage tolerance

1. Introduction

Hydrogen is emerging as a promising carbon-free energy carrier, but its deployment depends on lightweight and safe storage systems [1]. Composite pressure vessels, particularly those made from carbon fibre reinforced polymers (CFRPs), are therefore attractive because they offer significantly higher strength-to-weight ratios than conventional metal tanks [2]. Type V vessels eliminate the liner entirely and rely on the composite laminate both to support the pressure and to act as the hydrogen barrier [3]. For mobile and aerospace applications, hydrogen must be stored at very high pressures or cryogenic temperatures to achieve sufficient density [4]. Eliminating the liner could reduce tank weight but requires the composite laminate to maintain both barrier function and structural performance without forming through-thickness microcracks.

Micro-cracking in cryogenically cycled composite laminates is a well-recognized failure mechanism. When composites are subjected to cryogenic conditions, microcracks may form in the matrix due to thermal stresses caused by the mismatch in thermal expansion between the fibres and the polymer matrix [5–8]. Subsequent delamination between plies develops after a microcrack network has formed [9]. When microcracks and delamination coalesce, they create through-thickness leak paths that drastically increase hydrogen permeability [10–12] and degrade structural integrity[13,14]. Reusable cryogenic tanks designed for spacecraft and vehicles are therefore vulnerable to catastrophic leakage or structural failure once microcracks propagate through the laminate, highlighting the need for microcrack-resistant and repairable materials.

Self-healing materials have been developed to mitigate the accumulation of microcracks and extend the service life of structural composites. Self-healing strategies are generally classified as extrinsic or intrinsic, depending on how the healing capability is incorporated into the material [15]. In extrinsic systems, healing agents are stored in reservoirs such as microcapsules [16,17], hollow fibres [18,19] and vascular networks [20], and released when cracks rupture these reservoirs, enabling localised polymerisation within the damage zone. Despite their effectiveness, such systems are typically limited to a single healing event, as the encapsulated healing agent is consumed once released. This limitation restricts their applicability in reusable cryogenic

hydrogen storage tanks that experience repeated cryogenic thermal cycles. In contrast, intrinsic self-healing systems rely on the inherent characteristics of the polymer matrix. Healing may occur through reversible covalent reactions [21] or hydrogen bonds [22], or through physical mechanisms such as thermoplastic chain mobility [23–25]. In the latter case, heating above the melting temperature enables thermoplastics to melt and flow into the crack, where they solidify upon cooling and restore structural integrity. Because the healing mechanisms are reversible, intrinsic systems might enable multiple healing cycles under appropriate external stimuli.

Accordingly, thermoplastic-based interleaving and spray-coating have been explored as two routes for introducing self-healing functionality into CFRP laminates. In interleaved systems, a thermoplastic layer is inserted between adjacent plies, allowing the molten polymer to flow along the interlaminar crack plane and restore bonding upon cooling [26,27]. For example, polycaprolactone-interleaved continuous fibre reinforced polymer composites have been reported to heal by melting and filling damage [28], with healing efficiency dependent on interlayer content and healing time [29]. Earlier studies on poly (ethylene-*co*-methacrylic acid) (EMAA) based copolymer films also demonstrated combined interlaminar toughening and self-healing behaviour in carbon fibre (CF) reinforced epoxy laminates [30,31]. In spray-coated systems, a thermoplastic healing phase is deposited directly onto the fibre surface, where it can modify the fibre–matrix interface and provide a local healing source when remelted under thermal stimulation. An earlier study showed that spray-coated EMAA nanoparticles adhered well to carbon fibres, improving fracture toughness and enabling self-healing with over 40% fracture-toughness recovery across three repair cycles [32].

However, their relative performance under cryogenic conditions remains unclear. Introducing an additional thermoplastic phase as either an interleaf or a surface coating may potentially lead to local thermal-mismatch stresses, crack propagation, and interfacial damage. Therefore, performance established at ambient temperature cannot be assumed to translate directly to cryogenic conditions. For example, PES interleaves improved interlaminar fracture toughness at both 293 and 77 K, but the magnitude of improvement decreased from 76% to 48% at 77 K, showing that cryogenic conditions can change the effectiveness of the added phase [33]. For

cryogenic hydrogen tanks, this issue is particularly important because cryogenic temperature can increase leakage rate of hydrogen for a given damage state by opening crack junctions and ply-interface delamination [34,35]. It is therefore important to investigate how the placement of the thermoplastic healing phase influences both the cryogenic mechanical response of CFRP laminates and the efficiency of the subsequent healing process.

Although thermoplastic interleaving and fibre-surface coating have both been explored as routes for improving the damage tolerance of CFRP laminates, their relative performance under repeated cryogenic damage-healing conditions remains poorly understood. The influence of healing-phase architecture is particularly important for cryogenic composite structures, where thermal-mismatch stresses, matrix microcracking, and interlaminar damage can compromise residual mechanical performance. In this study, EMAA was incorporated into carbon fibre/epoxy laminates using two architectures with comparable healing-agent contents: a continuous mid-plane interleaf and a spray-coated particulate phase on the fibre surface. By comparing their monotonic and cyclic tensile responses at room temperature (RT) and under liquid-nitrogen immersion, this work clarifies the role of healing-phase architecture in governing cryogenic damage tolerance and mechanical recovery of self-healing CFRP laminates.

2. Materials and Manufacturing

2.1 Materials

The matrix system used throughout this work was Araldite® LY 564 epoxy resin cured with Aradur® 2954 hardener (Huntsman Corporation). The thermoplastic healing agent was EMAA in pellet form (Nucrel® 925, Dow) as shown in Figure 1a. This material was chosen for two main reasons. First, its melting temperature of approximately 92 °C is above the initial curing temperature of the epoxy system, thereby preventing premature melting and flow before matrix gelation. Second, EMAA has been reported to show good adhesion to CF surfaces [32]. The reinforcement was a 2 × 2 twill woven CF fabric (12k, 450 g/m²) supplied by Easy Composites

(UK), shown in Figure 1a. The woven fabric had an areal density of 450 g/m², corresponding to an approximate cured ply thickness of ~0.45 mm under typical resin-infusion conditions [36,37].

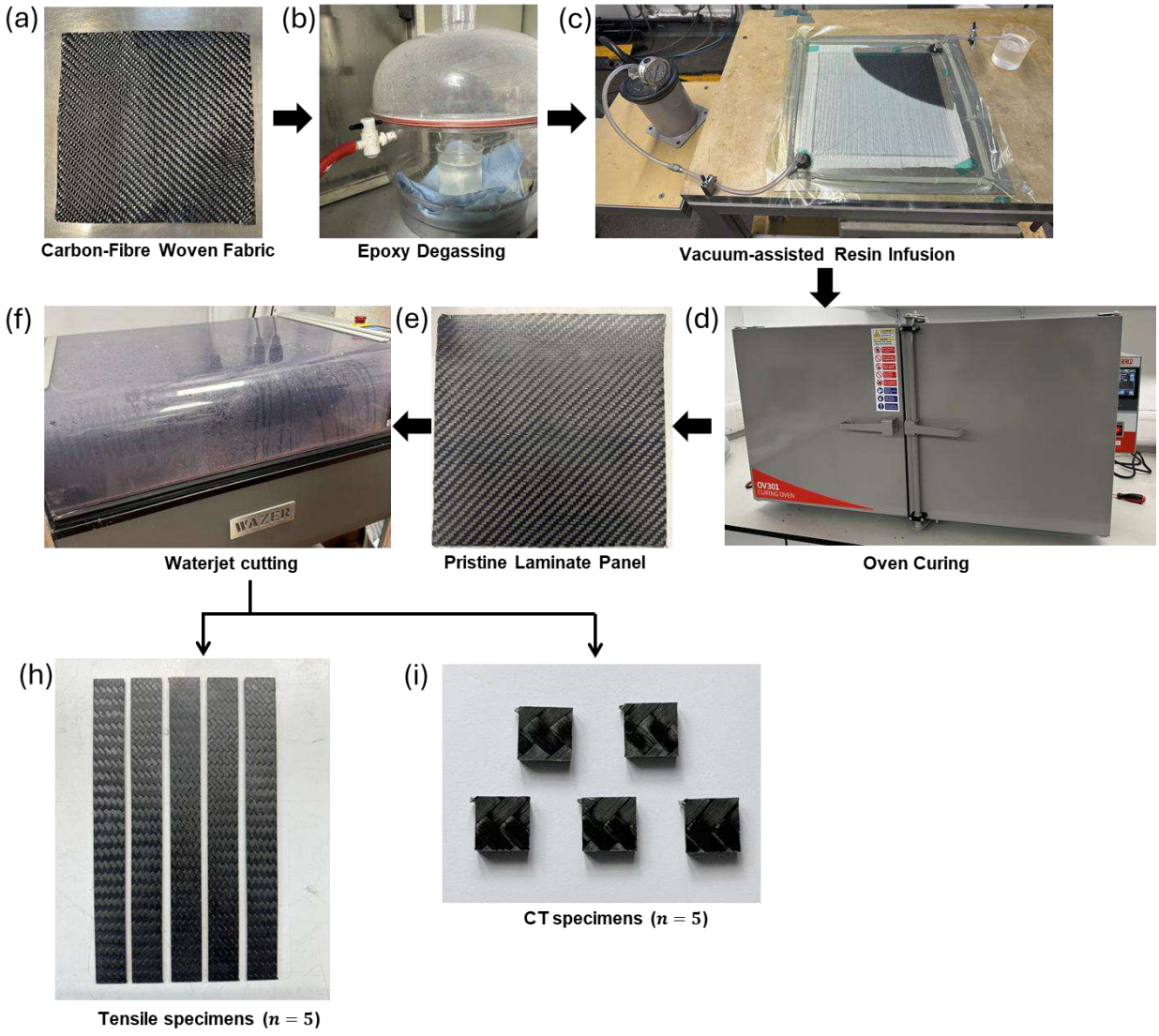


Figure 1. Fabrication routes for pristine CFRP laminates. (a) Carbon-fibre woven fabrics were stacked in a $[\pm 45^\circ]_6$ layup, followed by (b) epoxy degassing, (c) vacuum-assisted resin infusion, and (d) thermal curing. (e) The cured laminate panel was then sectioned by (f) waterjet cutting to obtain (h) tensile coupons and (i) CT specimens.

2.2 Manufacturing of test samples

2.2.1 Fabrication of pristine laminates

Six plies of CF fabric were then stacked, with the fabric yarns oriented at ±45° to the loading direction, to produce laminates with an approximate thickness of 2.5 - 3 mm, consistent with the specimen thickness requirements for tensile testing according to ASTM D3039 [38]. The epoxy resin and curing agent were mixed at a weight ratio of 100:35, in accordance with the manufacturer's recommendation, and degassed under vacuum (see Figure 1b) prior to infusion. Composite laminates were fabricated by vacuum-assisted resin infusion (VARI), as shown in Figure 1c. After infusion, the laminates were cured at 60 °C for 2 h followed by 120 °C for 6 h (Figure 1d). The cured laminate panels were then sectioned using a waterjet cutter (WAZER, USA) to prepare five tensile specimens with dimensions of 250 mm × 25 mm (Figure 1h) and five CT specimens with dimensions of 10 mm × 10 mm for internal-structure analysis (Figure 1i).

2.2.2 Fabrication of interleaved self-healing (ISH) laminates

The EMAA mass and film thickness were selected to balance healing functionality and laminate integrity. EMAA pellets (Figure 2a) were compression-moulded into interleaf films (Figure 2c) using a Collin P3100 E hot press at 150 °C for 2 min under 240 bars, producing films with a thickness of 0.21 ± 0.02 mm measured by a digital micrometre (IP65, Mitutoyo, Japan). This thickness was selected to provide a continuous thermoplastic healing layer while remaining less than half of the nominal cured carbon-fibre ply thickness (~0.45 mm), thereby limiting the introduction of an excessively thick compliant interlayer. A 280 × 280 mm² interleaf region consisting of about 15 g EMAA was placed at the mid-plane within a 300 × 300 mm² six-ply [±45] CF preform in the stacking sequence of [CF_3/EMAA/CF_3] as illustrated in Figure 2d. To promote resin infusion through the thickness during VARI, a 10 mm gap was left between the interleaf edge and the laminate boundary, as illustrated in Figure 2d. The laminates were subsequently infused and cured at 60 °C for 2 h followed by 120 °C for 6 h. The architecture of ISH laminate is illustrated in Figure 2e.

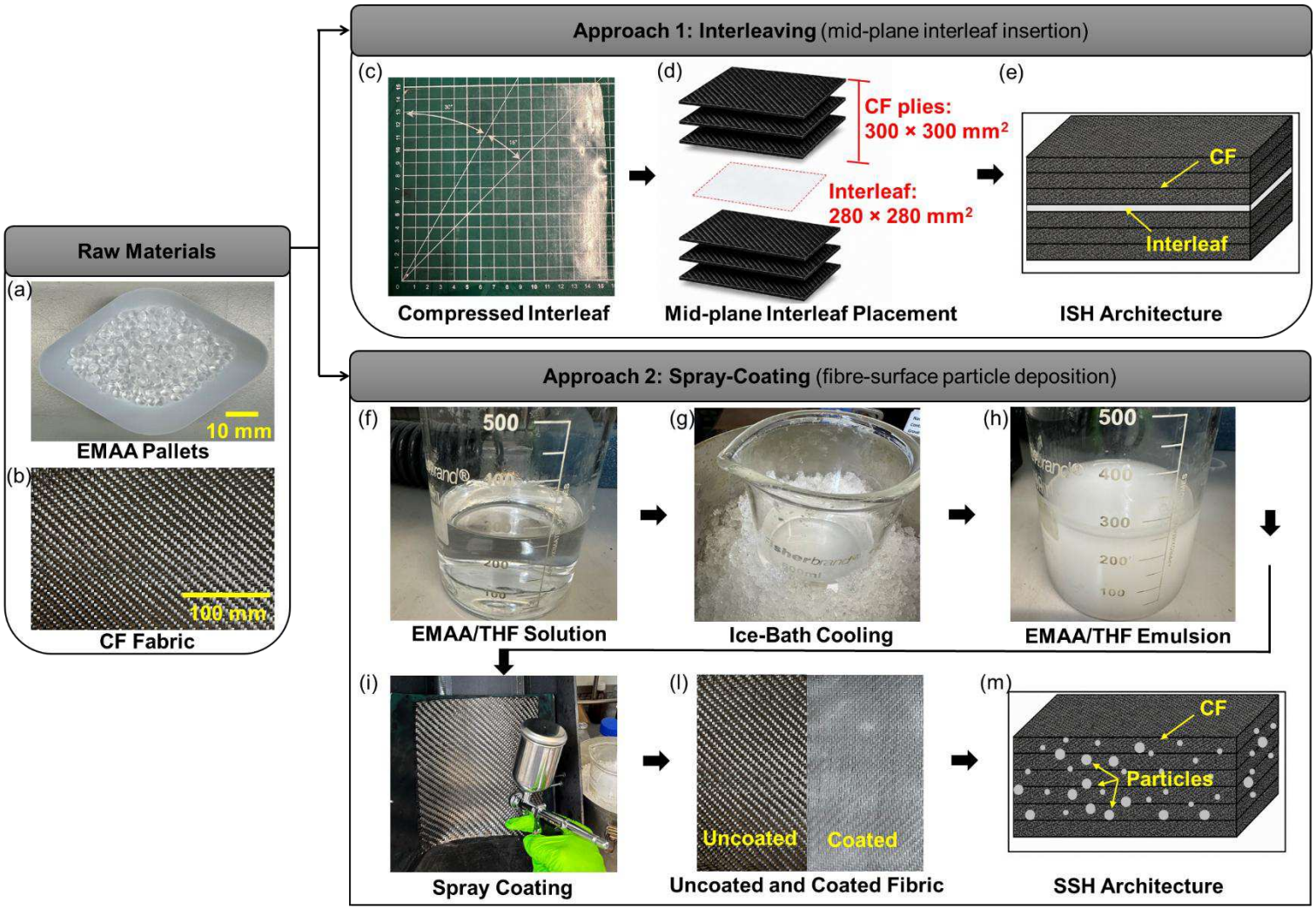


Figure 2. Fabrication routes for EMAA-modified self-healing CFRP laminates. (a, b) Raw materials. (c–e) Interleaving route, including EMAA film preparation, mid-plane interleaf placement, and the interleaved laminate architecture. (f–j) Spray-coating route, including EMAA/THF emulsion preparation, fibre-surface coating, and the spray-coated laminate architecture.

2.3 Fabrication of spray-coated self-healing (SSH) laminates

EMAA pellets were dissolved in tetrahydrofuran (THF) at 60 °C under magnetic stirring at a concentration of 0.016 g/mL. The solution (Figure 2f) was subsequently cooled in an ice bath (Figure 2g) until a white emulsion formed (Figure 2h), which was then spray-coated onto both sides of the carbon-fibre woven fabrics using an air-pressure spray gun with a 0.6 mm nozzle (HP-TH2 Airbrush, Anest Iwata Corporation, Japan), as shown in Figure 2i. The spray coating was conducted at an approximate stand-off distance of 15 cm and an air pressure of 20 psi until approximately 15 g of EMAA, equal to the mass used for the interleaved laminate, was deposited over the six CF plies to enable a direct comparison between the interleaved and spray-coated architectures. After spray coating, the woven fabrics (Figure 2l) were dried in a fume hood under circulating air for 12 h prior to resin infusion to ensure removal of residual THF. The spray-coated preforms were then infused and cured using the same procedure as that used for the pristine laminates. The architecture of SSH laminate is illustrated in Figure 2m.

3. Evaluation of tensile properties and healing efficiency

The specimen dimensions (250 mm × 25 mmm, shown in Figure 3a) for the tensile tests were selected in accordance with ASTM D3039. In addition, all five specimens for each condition were extracted from the same laminate to minimise experimental scatter and ensure consistency in material properties.

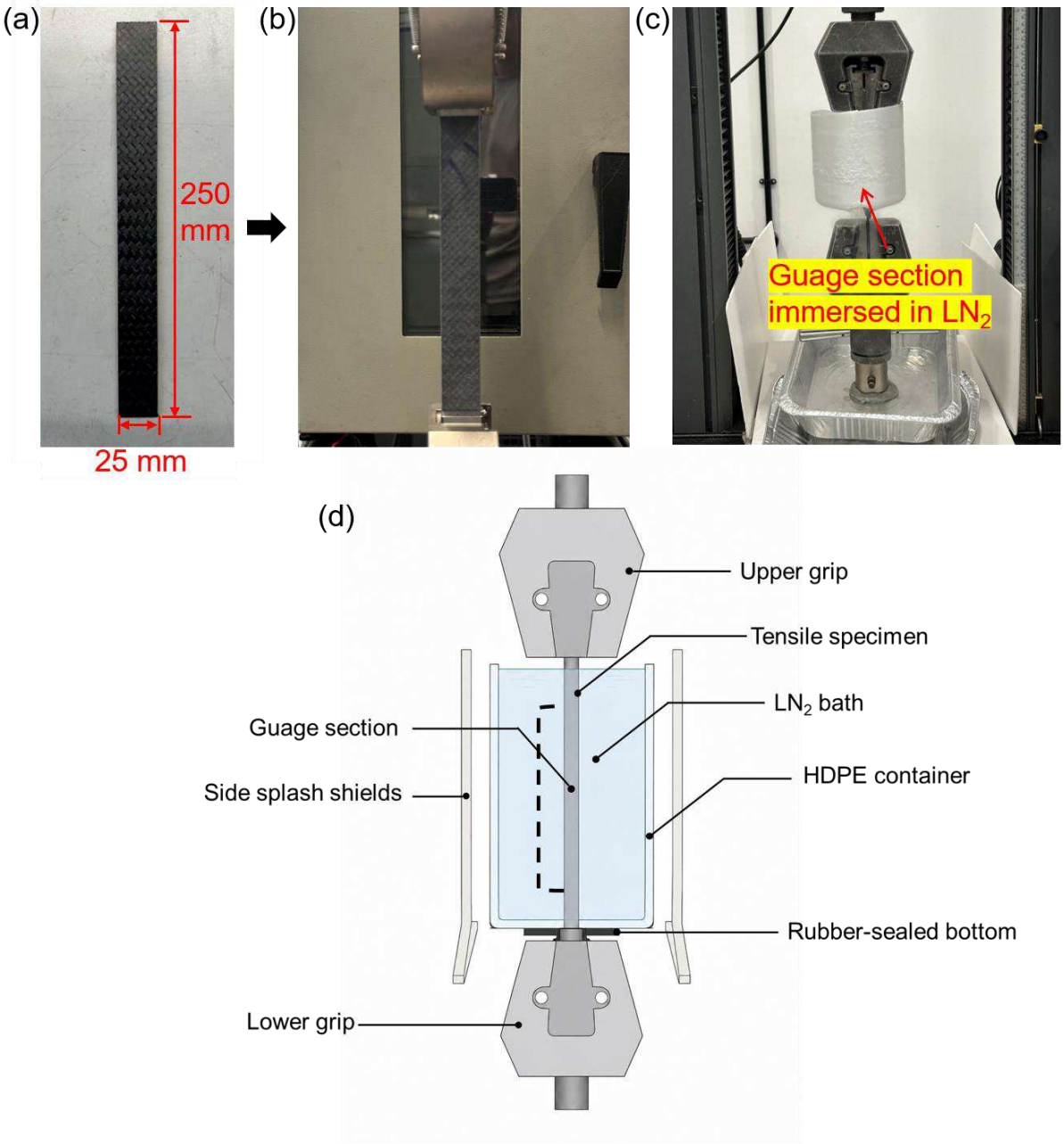


Figure 3. Tensile testing configuration and cyclic loading–healing protocol. (a) Tensile specimen used for mechanical testing. Experimental setup under (b) room-temperature and (c) cryogenic conditions. (d) Schematic of the cryogenic tensile setup with specimen's gauge section fully immersed in liquid nitrogen.

3.1 Monotonic tensile test

The effect of EMAA healing agents, introduced via the two methods, on the mechanical properties was evaluated using monotonic tensile tests performed until failure. The woven carbon-fibre yarns

were oriented at ±45° to the loading direction. This configuration was selected because tensile loading in the ±45° orientation promotes matrix- and interface-dominated deformation, making the laminate more sensitive to stiffness degradation and therefore suitable for evaluating the influence of the healing phase on damage development and mechanical recovery.

Tensile tests were conducted using an Instron 5569 universal testing machine equipped with a 30 kN load cell under both RT (Figure 3b) and cryogenic conditions (Figure 3c). For cryogenic testing, the gauge section of each specimen was immersed in liquid nitrogen using an HDPE container with a rubber-sealed bottom, as illustrated in Figure 3d. The specimen was held in liquid nitrogen for 10 min before loading and remained immersed throughout the test, corresponding to a test temperature of approximately −196 °C. The 10 min pre-immersion time was selected to promote thermal equilibrium within the specimen. This duration was chosen based on a previous study showing that an approximately 1 mm thick CFRP specimen reached −196 °C within about 2 min and that the cooling time increased approximately linearly with specimen thickness [9]. Based on this, the centre of the present about 3.0 mm thick specimens was estimated to reach −196 °C within approximately 6 min; therefore, a 10 min holding time was used to provide an additional margin for thermal stabilisation. All specimens were loaded to failure at a crosshead speed of 2 mm min^{-1}.

3.2 Cyclic tensile test and healing performance

Cyclic tensile tests were conducted under displacement control using the Instron 5569 system to evaluate damage accumulation and stiffness recovery. Four loading-healing cycles were applied to each specimen. The strain level used for the first loading cycle was selected from the monotonic tensile response of each laminate system. As recommended in ASTM D3039, the transition strain was identified as the midpoint of the nonlinear transition region in the engineering stress–strain curve, where a clear reduction in slope indicated the onset of matrix- and interface-dominated damage, as illustrated in Figure 4a. This transition strain was therefore used as a practical damage-initiation criterion for defining the first cyclic loading level. Based on the monotonic tensile curves, the transition strain was determined as 2.5% for the pristine laminate and 3.75% for both self-healing laminates at room temperature, and 1.0% for all laminates under cryogenic conditions.

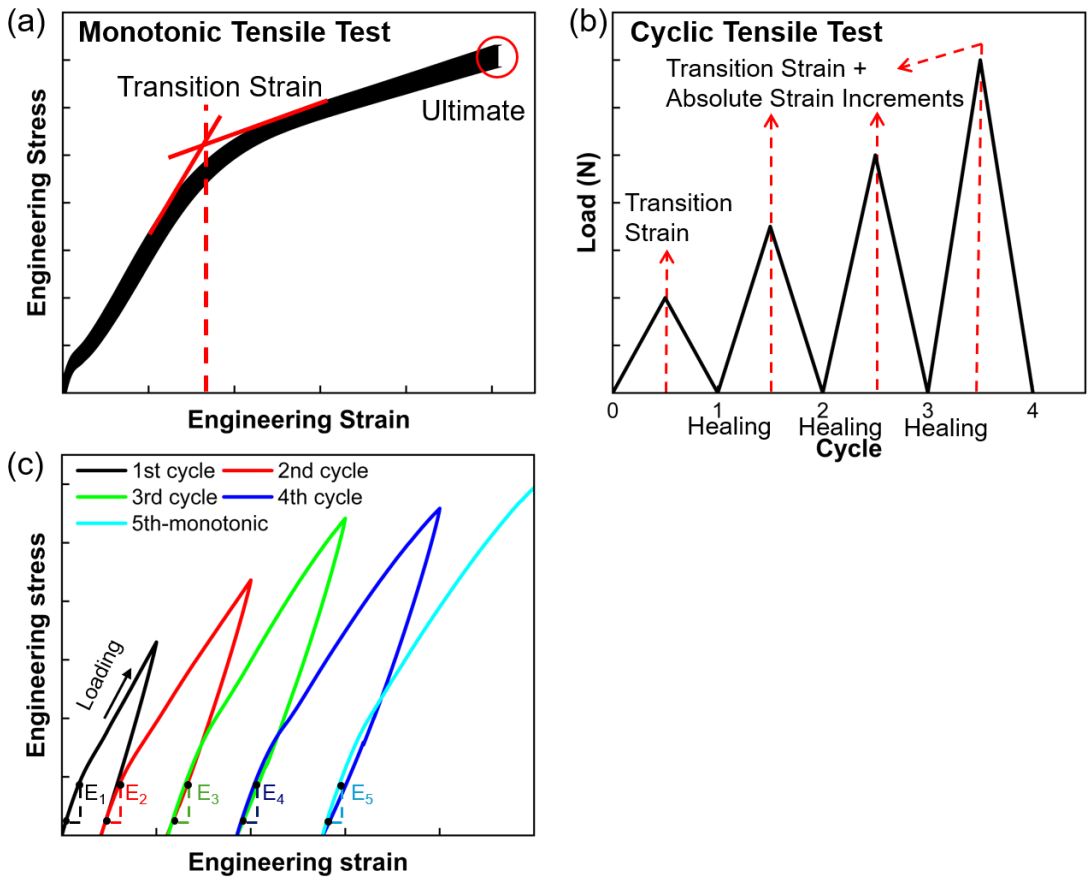


Figure 4. Schematic illustration of the cyclic tensile loading-healing analysis. (a) Determination of the transition strain from the monotonic engineering stress–strain response. (b) Cyclic tensile loading-healing protocol. (c) Calculation of stiffness retention from the tensile modulus measured in each loading cycle.

The cyclic loading-healing protocol is illustrated in Figure 4b. In the first cycle, each specimen was loaded to the corresponding transition strain and then unloaded to zero load. In subsequent cycles, the peak strain was progressively increased by a fixed absolute strain increment to introduce increasing levels of damage and evaluate stiffness retention after repeated healing. The strain increment was set to 2.0% at room temperature and 1.0% under cryogenic conditions, reflecting the narrower deformation window and more brittle response of the laminates at low temperature. After each loading cycle, the self-healing specimens (ISH and SSH) were removed from the tensile testing setup and thermally healed at 150 °C for 1 h under a pressure of 5 bar using

a Collin P3100 E hot press. The healed specimen was then returned to the setup and reloaded under the same testing condition in the subsequent cycle.

The healing performance was quantified in terms of stiffness retention, R_i, defined as the ratio between the tensile modulus after cycle i and the initial modulus measured during the first loading cycle. It was calculated as:

$$R_i = \frac{E_i}{E_1} \times 100\%$$

where E_i and E_1 are the tensile modulus measured in cycle i and in the first loading cycle, respectively, as illustrated in Figure 4c. The tensile modulus was calculated from the slope of the initial linear region of the engineering stress–strain curve. Engineering stress was calculated by dividing the applied load by the initial cross-sectional area of the specimen, while engineering strain was estimated by normalising the crosshead displacement recorded by the Instron testing machine by the initial gauge length. Direct strain measurement using a video extensometer or strain gauge was not feasible during liquid-nitrogen immersion. Therefore, the reported strain and tensile modulus values should be interpreted as apparent values, because the measured displacement includes contributions from both specimen deformation and system compliance associated with both upper and lower grips. However, as the Young's moduli of the test samples (~ 15 GPa) are much smaller than that of the material for grips in the tensile test machine (> 110 GPa), the measured displacements by the load cell come mainly from the test samples. After the completion of the fourth loading-healing cycle, the specimens were finally reloaded monotonically to failure to evaluate the influence of repeated damage and healing on strength and ductility. It is worth noting that for each condition, five specimens were extracted from the same laminate and tested to ensure consistency across tests.

3.3 Morphological characterization

The surface morphology of the spray-coated carbon-fibre fabrics was characterised using scanning electron microscopy (SEM) with an Inspect F microscope (FEI, USA). The size distribution of the deposited EMAA particles was determined from SEM images using ImageJ software [39]. The internal structures of the samples were observed by CT scan using a PE 4343 scanner (PerkinElmer, USA) with a voxel size of 4.5 μm. The thickness of the interleaf in the cured laminate was measured from CT-scan images using ImageJ software.

4. Results and discussion

4.1 The compositions and structure of the fabricated laminates

Constituent contents of the pristine and self-healing laminates were compared prior to mechanical testing. Because EMAA integration (interleaving or spray coating) modifies the relative fractions of fibre and matrix, it can inherently affect the baseline stiffness and strength. Table 1 summarises the measured constituent mass fractions of the pristine, ISH, and SSH laminates. The values represent the average of four laminates fabricated for monotonic and cyclic tensile testing under both RT and cryogenic conditions. As expected, the pristine laminates consisted only of fibre and epoxy, with mass fractions of 69.3 ± 0.1 wt% and 30.7 ± 0.1 wt%, respectively. After incorporation of the healing phase, both self-healing laminates exhibited comparable EMAA contents, i.e., 3.8 ± 0.2 wt% for ISH and 3.6 ± 0.2 wt% for SSH.

Table 1. Constituent mass fractions of the laminates

Samples	EMAA (wt%)	Epoxy (wt%)	Fibre (wt%)
Pristine	NA	30.7 ± 0.1	69.3 ± 0.1
ISH	3.8 ± 0.2	35.9 ± 1.2	60.3 ± 1.0
SSH	3.6 ± 0.2	37.0 ± 1.5	59.5 ± 1.3

In both self-healing laminates, the introduction of EMAA was accompanied by a reduction in fibre content and a corresponding increase in matrix content relative to the pristine laminate. Compared

with the pristine laminate, the fibre mass fraction decreased by 13.0% in ISH and 14.1% in SSH, whereas the epoxy mass fraction increased by 16.9% and 20.5%, respectively. Although the two self-healing routes introduced the healing phase in different forms, their overall constituent contents were relatively comparable. Accordingly, differences in tensile response between ISH and SSH can be mainly associated with variations in healing-phase distribution and laminate morphology.

Figure 5 compares the internal morphology of the pristine, ISH, and SSH laminates. The CT image of the pristine laminate (Figure 5a) shows a relatively uniform through-thickness structure without any distinct localised matrix-rich band. In contrast, the ISH laminate (Figure 5b) exhibits a clearly identifiable mid-plane interleaf, together with localised resin-rich regions adjacent to the interleaf. This morphology may result from the continuous EMAA film partially restricting through-thickness resin flow during VARI, leading to local resin accumulation around the interleaf. The thickness of the interleaf in the cured laminate was 271 ± 11 μm, which was comparable to the initial film thickness before curing. This indicates that the EMAA interleaf largely retained its original geometry and thickness during resin infusion and curing, with limited squeezing, dissolution, or redistribution into the surrounding laminate. In contrast, the SSH laminate (Figure 5c) exhibits a more distributed morphology, where matrix/healing-phase-rich regions are dispersed between neighbouring plies rather than concentrated at a single mid-plane interleaf. This difference is consistent with the two different routes incorporating self-healing phase, namely a continuous mid-plane interleaf in ISH and particle deposition on the surface of fibre tows in SSH. SEM observations further confirm the morphology of the spray-coated preform. As shown in Figure 5d-e, EMAA particles were successfully deposited onto the carbon-fibre tow surfaces, despite some particle agglomerations. Gaussian fitting of the particle-size distribution (Figure 4f) gave an average particle diameter of 7.1 ± 3.6 μm.

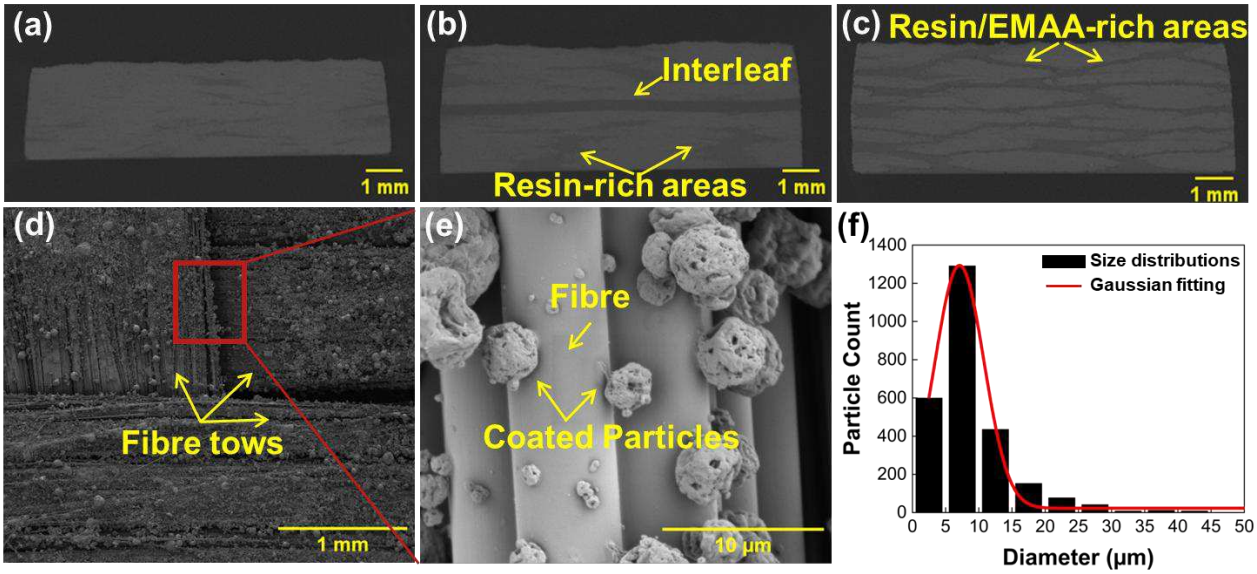


Figure 5. Morphological characterization of the pristine and self-healing laminates before testing. (a–c) X-ray CT images of the pristine, interleaved self-healing (ISH), and spray-coated self-healing (SSH) laminates, respectively. (d, e) SEM images of EMAA particles deposited on the carbon-fibre woven preform after spray coating at different magnifications. (f) Particle size distribution of the spray-coated EMAA particles, showing a Gaussian-fitted average diameter of 7.1 ± 3.6 µm.

These results indicate that the two self-healing laminates contained similar EMAA mass fractions but exhibited markedly different healing-phase distributions. ISH contained a localised mid-plane interleaf associated with concentrated resin-rich regions, whereas SSH contained discrete micro-particles deposited on fibre surfaces with more distributed resin/EMAA-rich regions between plies across the structure.

4.2 Monolithic tensile properties under RT and cryogenic conditions

The stress–strain responses of the pristine, ISH, and SSH specimens subjected to monotonic tensile loading under RT and cryogenic conditions are compared in Figure 6 to evaluate the effects of healing agents and incorporation routes on mechanical performance. The tensile properties are summarised in Table 2.

Table 2. Tensile properties of pristine and self-healing specimens under RT and cryogenic conditions.

Specimen	Young's modulus (GPa)		Tensile strength (MPa)		Strain to failure (%)	
	RT	Cryogenic	RT	Cryogenic	RT	Cryogenic
Pristine	11.1 ± 0.6	13.3 ± 1.7	164.2 ± 1.8	166.5 ± 3.1	10.1 ± 0.3	4.4 ± 0.5
ISH	7.4 ± 0.2	11.0 ± 1.8	146.2 ± 4.1	151.9 ± 9.6	11.2 ± 1.4	4.2 ± 0.6
SSH	6.5 ± 0.5	10.9 ± 1.3	138.9 ± 2.1	166.3 ± 16.8	11.8 ± 0.5	4.1 ± 0.4

Under RT (Figure 6a), all the samples s exhibited ductile tensile performance. The incorporation of EMAA reduced both the stiffness and tensile strength compared with the pristine sample. As shown in Figure 6c-d, the pristine specimen exhibited the highest Young's modulus and tensile strength, reaching 11.1 ± 0.6 GPa and 164.2 ± 1.8 MPa, respectively. In contrast, both self-healing specimens showed lower stiffness and strength, with the modulus decreasing to 7.4 ± 0.2 GPa for ISH and 6.5 ± 0.5 GPa for SSH, and the strength decreasing to 146.2 ± 4.1 MPa and 138.9 ± 2.1 MPa, respectively. This reduction is consistent with the constituent and morphological results discussed above, i.e., the lower fibre mass fraction, more matrix-rich regions, and the introduction of a compliant thermoplastic phase in the self-healing specimens. By contrast, the elongation of the self-healing specimens under RT was slightly higher than that of the pristine specimen, increasing from 10.1 ± 0.3% in the pristine specimen to 11.2 ± 1.4% in ISH and 11.8 ± 0.5% in SSH. This suggests that incorporation of EMAA increased the deformability of the CFRP composite under tensile loading, which is consistent with the softer and more ductile nature of the thermoplastic phase [40,41].

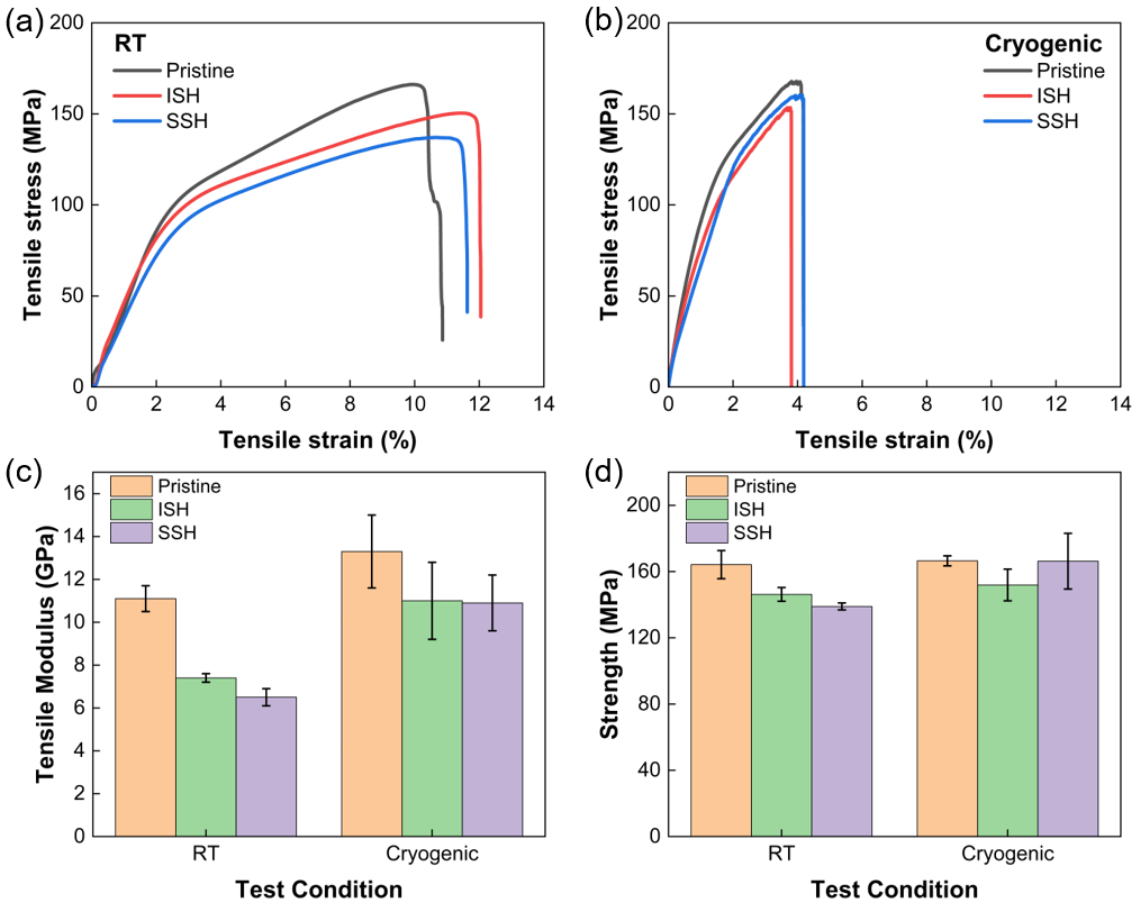


Figure 6. Representative stress–strain curves of specimens subjected to ±45° monotonic tensile loading under RT (a) and cryogenic (b) conditions. The tensile modulus (c) and the strength (d) of specimens under the two test conditions.

Under cryogenic conditions (Figure 6b), all specimens exhibited brittle tensile performance with a significant increase in stiffness, as well as a reduction in elongation at failure. As shown in Figure 6c-d, the Young's modulus increased from 11.1 ± 0.6 GPa to 13.3 ± 1.7 GPa in the pristine specimen, corresponding to a relative increase of 20%. More significant increases were observed for the self-healing specimens, i.e., 49% for ISH and 68% for SSH, corresponding to cryogenic moduli of 11.0 ± 1.8 GPa and 10.9 ± 1.3 GPa, respectively. A similar trend was observed in tensile strength, although the magnitude of increase was smaller for the pristine (1%) and ISH (4%) specimens and much larger for SSH (20%). Notably, the cryogenic strength of SSH increased to 166.3 ± 16.8 MPa, which was comparable to that of the pristine specimen (166.5 ± 3.1 MPa). In contrast, the strain at failure decreased for all specimens, from 10.1–11.8% at RT to 4.1–4.4% at

cryogenic temperature, corresponding to reductions of 56–65%. These changes confirm that the specimens became significantly more brittle at cryogenic temperature.

The overall cryogenic response can be attributed to reduced molecular mobility of the epoxy matrix and increased constraint at the fibre-matrix interface at low temperature, which enhance load transfer and raise the apparent stiffness of the specimen. In the present ±45° woven configuration, the tensile response is strongly influenced by matrix- and interface-dominated deformation; accordingly, the stiffening effect of cryogenic condition is particularly pronounced. At the same time, the sharp reduction in elongation indicates that the ability of the matrix to accommodate deformation was reduced, promoting more brittle failure. The larger modulus increase observed in ISH and SSH relative to the pristine specimen suggests that the added EMAA phase and associated matrix-rich regions were especially sensitive to cryogenic stiffening.

However, the two self-healing architectures responded differently in strength. While ISH remained weaker than the pristine specimen, SSH exhibited similar cryogenic tensile strength as the pristine specimen. This difference may be associated with the distinct distribution of the healing phase. At room temperature, the compliant EMAA deposited on fibre surfaces in SSH might reduce interfacial load-transfer efficiency over a larger proportion of the specimen, which may account for its lower tensile strength compared with ISH. In contrast, the EMAA in ISH is primarily confined to a discrete mid-plane interleaf, so its influence on the tensile load-bearing architecture is more localised and therefore less detrimental to the RT strength. Under cryogenic conditions, however, cryogenic stiffening of the EMAA-modified interfacial region in SSH may reduce this local compliance and promote more effective stress transfer to the fibres, which may contribute to the larger increase in tensile strength. By comparison, although the interleaf in ISH also becomes stiffer at low temperature, it remains concentrated as a localised mid-plane heterogeneity rather than acting as a distributed interfacial modifier. As a result, the interleaf in ISH may contribute less effectively to tensile strengthening under cryogenic loading.

4.3 Cyclic tensile properties and residual tensile performance after repeated healing

The cyclic strain ranges were defined from the monotonic tensile responses under the corresponding test conditions. In each case, the first cycle was terminated at the transition strain, and the peak strain in subsequent cycles was progressively increased. At room temperature, the transition strain was 2.5% for the pristine specimen and 3.75% for both self-healing specimens. Therefore, an absolute increment of 2.0% was used in the subsequent cycles so that the cyclic loading range spanned the maximum strain window observed in the monotonic tests (about 10–12%, Table 2). Under cryogenic conditions, the transition strain was 1.0% for all specimens, and the increment was reduced to 1% to match the narrower strain window (up to 4.0%).

4.3.1 Cyclic responses under RT conditions

Figure 7a-c shows the cyclic tensile response of the specimens under RT conditions. In all cases, the starting points of loading-unloading loops progressively shifted to higher strain, indicating the accumulation of irreversible deformation during repeated cycling. Because the peak strain in each cycle was intentionally increased from the previous cycles, the increase in peak stress the cycle should not be interpreted as improved mechanical performance. Instead, the evolution of tensile modulus and stiffness retention provides the more meaningful measure of damage accumulation and structural recovery.

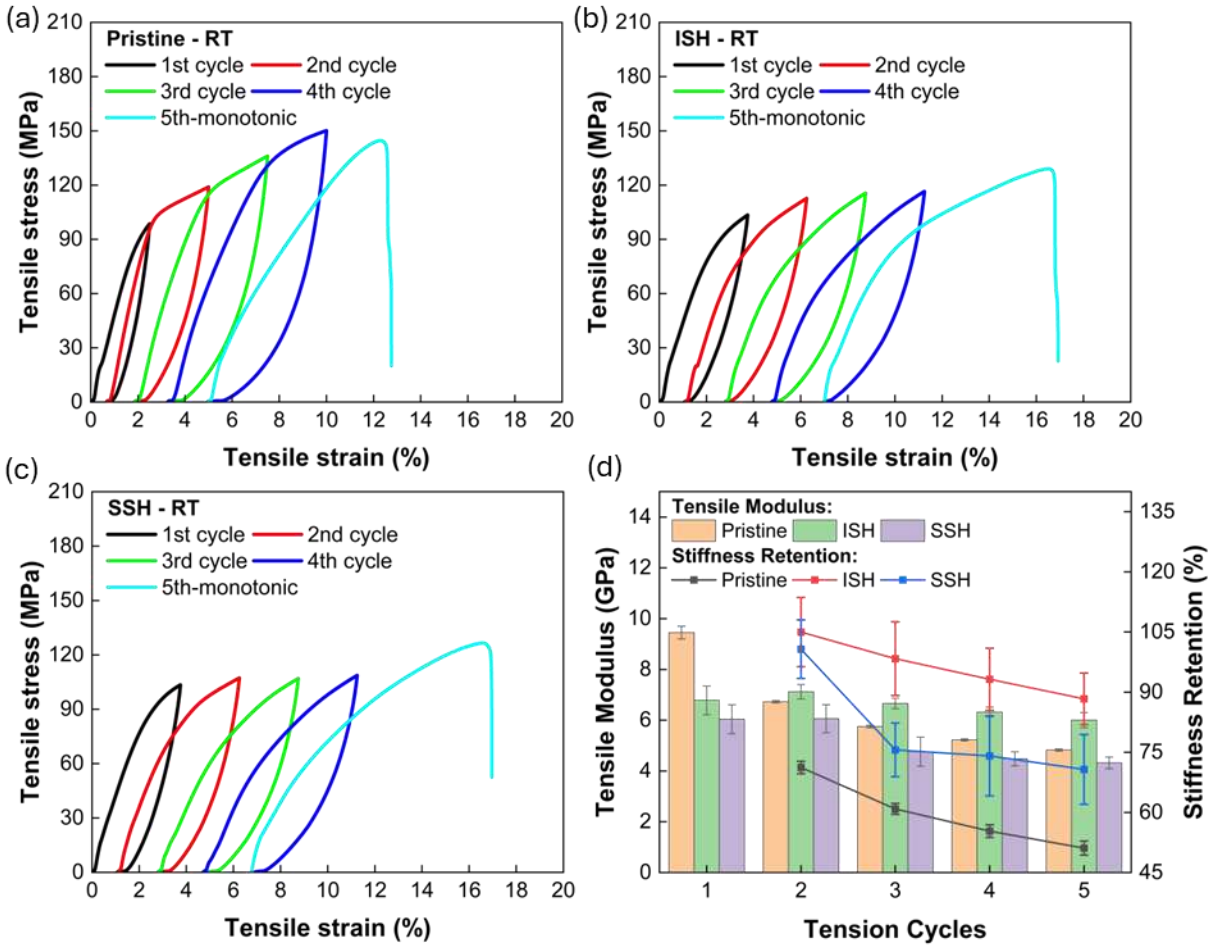


Figure 7. (a–c) Representative tensile stress–strain curves of the specimens under cyclic loading at RT; (d) evolution of tensile modulus and stiffness retention with increasing cycle number.

At RT, the pristine laminate exhibited the most pronounced stiffness degradation as illustrated in Figure 7d. Its modulus retention decreased continuously to 51.1 ± 1.8% by the final cycle. In contrast, both self-healing laminates retained stiffness more effectively, with ISH showing the most stable response and SSH an intermediate behaviour. By the final cycle, ISH retained 88.3 ± 6.4% of its initial modulus, whereas SSH retained 70.7 ± 8.7%. The slight modulus retentions above 100% observed for ISH and SSH in the early cycles can be interpreted as complete recovery within experimental scatter.

This trend is consistent with the structural differences described in Section 3.1. The EMAA-rich regions, being more compliant than the surrounding epoxy matrix and fibres, may serve as preferential sites for local deformation accumulation during cyclic loading. In ISH, EMAA is concentrated as a continuous mid-plane interleaf, providing a localised and continuous healing source at the dominant interlaminar damage zone. In SSH, by contrast, EMAA is distributed as discrete particles on fibre surfaces. Although this architecture provides a more spatially distributed healing phase, it is less effective than the continuous interleaf in repeatedly restoring stiffness once damage becomes concentrated along a critical crack path.

The final loading cycles in Figure 7a–c also show the residual tensile response after four cyclic loading-healing cycles. The residual strengths were 144.3 ± 2.3 MPa for the pristine laminate, 129.4 ± 4.3 MPa for ISH, and 128.2 ± 2.3 MPa for SSH, corresponding to approximate strength retentions of 87.9%, 88.5%, and 92.3%, respectively, relative to their corresponding monotonic tensile strengths presented in Section 3.2. These results indicate that the self-healing laminates did not show a substantial advantage over the pristine laminate in final RT residual strength. Instead, the benefit of EMAA incorporation at RT is more clearly observed in the improved cyclic stiffness retention than in the final strength to failure. The residual strengths of ISH and SSH were also similar, suggesting that the effect of healing-phase architecture was less pronounced in the final RT strength than in the cyclic modulus evolution. Nevertheless, both self-healing laminates exhibited higher total tensile strain at final failure than the pristine laminate, increasing from 12.3 ± 0.6% to 17.0 ± 1.0% for ISH and 17.7 ± 0.7% for SSH, indicating that the self-healing mechanisms increase ductility.

4.3.2 Cyclic responses under cryogenic conditions

Figure 8a–c presents the cyclic tensile responses of the pristine, ISH, and SSH laminates under cryogenic conditions. All specimens exhibited steeper stress–strain curves and a narrower deformation window than those tested at RT, consistent with the increased stiffness and reduced failure strain observed in the monotonic tensile tests. To accommodate this brittle response, the

peak strain increment under cryogenic conditions was set to 1.0% per cycle. Therefore, the following analysis focuses on the relative performance of the three laminate architectures under the same cryogenic loading protocol.

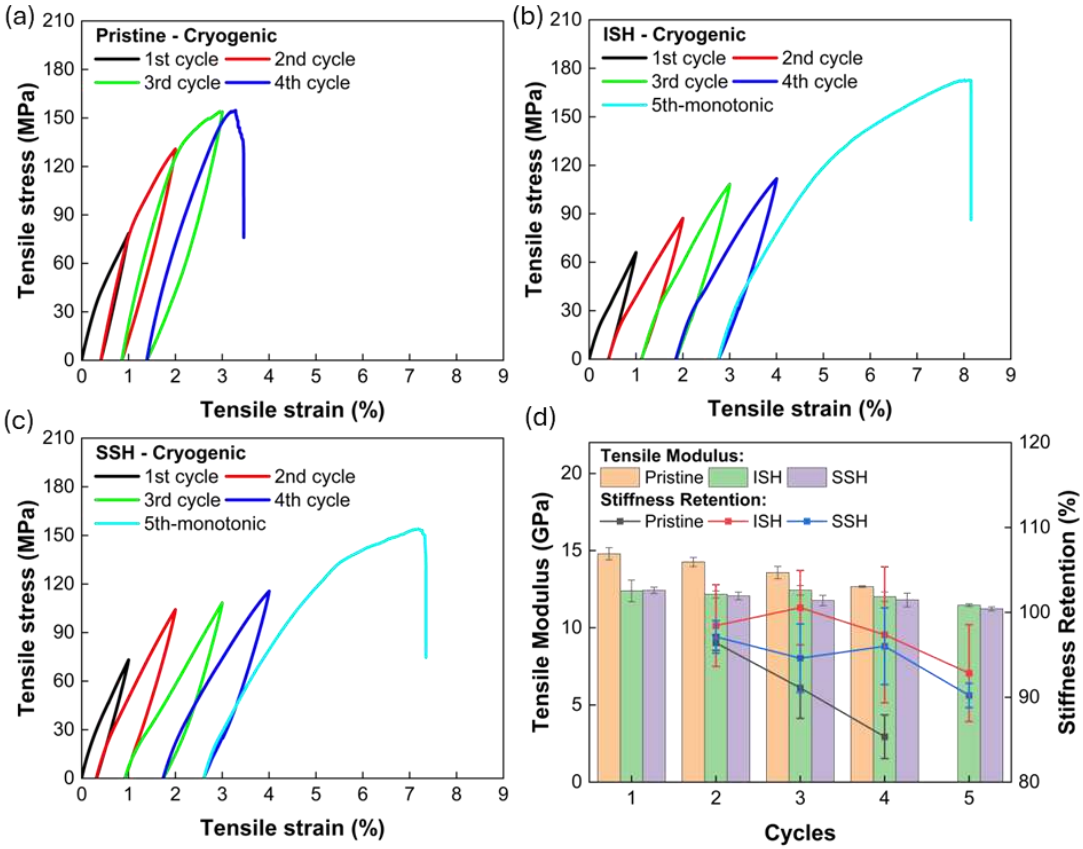


Figure 8. (a–c) Representative tensile stress–strain curves of the specimens under cryogenic cyclic loading; (d) evolution of tensile modulus and stiffness retention with increasing cycle number.

As shown in Figure 8d, the pristine specimens exhibited progressive stiffness degradation and failed either during the third or fourth loading cycle. For the pristine group, the last measurable modulus before failure corresponded to 84.3 ± 2.9% of the initial modulus, and no fifth-cycle modulus is reported because all pristine specimens failed before reaching the fifth cycle. In contrast, all ISH and SSH specimens completed the prescribed four loading-healing cycles and were subsequently loaded to final failure. By the final cycle, ISH and SSH retained 92.8 ± 5.7% and 90.2 ± 1.4% of their initial tensile modulus, respectively. Thus, under cryogenic loading, both

EMAA-based architectures reduced cyclic stiffness loss and improved resistance to premature failure relative to the pristine specimens. At the same time, the difference between ISH and SSH was smaller than that observed at RT, suggesting that once the EMAA-rich regions had stiffened at low temperature, the specific spatial distribution of the healing phase may have a weaker influence on cyclic modulus retention.

Because the pristine specimens failed during the cryogenic cyclic loading sequence, their residual strength was defined as the tensile strength measured at the cycle in which failure occurred. The pristine laminate retained 153.9 ± 6.8 MPa after cryogenic cyclic loading, corresponding to 92.4% of its original monotonic cryogenic strength. The SSH laminate showed a comparable residual strength of 152.9 ± 5.1 MPa, corresponding to 91.9% retention. In contrast, the ISH laminate reached the highest residual strength of 171.2 ± 2.4 MPa, corresponding to an apparent strength retention of 112.7% relative to its monotonic cryogenic reference. Notably, although ISH exhibited a lower initial monotonic cryogenic strength than both the pristine and SSH laminates, it outperformed both systems after repeated cryogenic loading-healing cycles. The residual strength of ISH was approximately 11.2% higher than that of the pristine laminate and 12.0% higher than that of SSH, indicating that the continuous EMAA interleaf was particularly effective in preserving load-bearing capacity after repeated cryogenic damage and thermal healing. Both self-healing laminates also exhibited higher total tensile strain at final failure than the pristine laminate. Relative to the pristine value of 3.3 ± 0.5%, the total tensile strain at final failure increased to 8.2 ± 0.1% for ISH and 7.2 ± 0.4% for SSH, corresponding to increases of approximately 148.5% and 118.2%, respectively.

Macroscopic observations after cyclic loading-healing further confirmed the thermal mobility of EMAA in the self-healing specimens (Figure 9). In the ISH specimen, local squeezed-out EMAA was observed near the specimen edge, indicating that the continuous interleaf underwent partial flow under the combined effect of temperature and pressure during healing. In the SSH specimen, EMAA-rich regions were observed on the specimen surface, suggesting local redistribution and coalescence of the spray-coated EMAA phase. These observations support the interpretation that

EMAA was thermally activated during the healing treatment and contributed to crack bridging, partial crack closure, and improved residual mechanical performance.

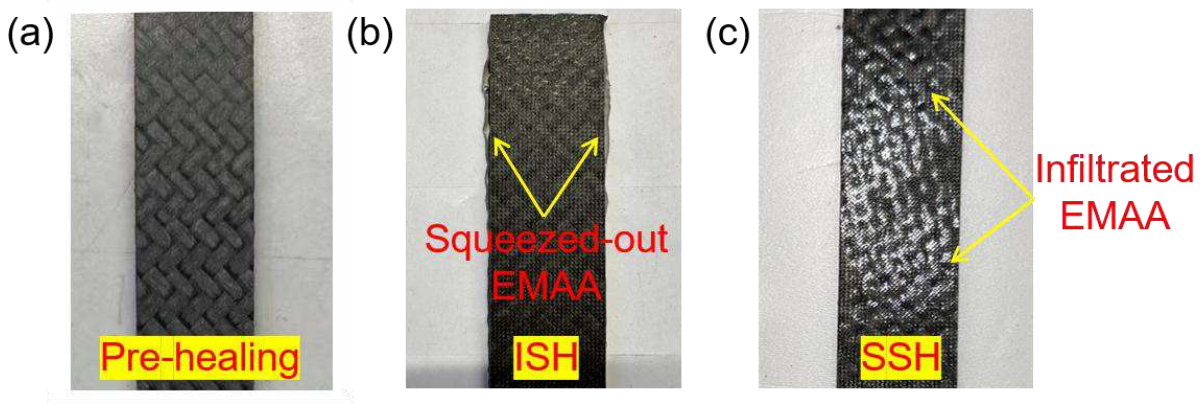


Figure 9. Macroscopic evidence of EMAA redistribution after thermal healing. (a) Surface appearance of a self-healing specimen before healing (pre-healing condition. (b) Squeezed-out EMAA observed near the edge of the ISH specimen after healing. (c) Infiltrated EMAA observed on the surface of the SSH specimen after healing.

Macroscopic observations further confirmed the thermal mobility of EMAA during the healing process (Figure 9). Compared with the specimen before healing, the ISH specimen showed squeezed-out EMAA near the specimen edge after thermal healing, indicating partial flow of the continuous interleaf under the combined effects of temperature and pressure. For the SSH specimen, local infiltrated EMAA was observed on the specimen surface after healing, suggesting redistribution of the thermoplastic phase from the internal fibre/coating region toward the surface during thermal activation. These observations support the role of EMAA flow and redistribution in crack bridging, partial crack closure, and residual mechanical recovery during repeated loading-healing cycles.

To further examine the damage mechanisms responsible for the different residual tensile responses, microscopic damage analysis was conducted on the failed tensile specimens after cryogenic cyclic testing. Macroscopic inspection was first used to define the region for cross-sectional SEM analysis. As shown in Figure 10, explosive delamination developed within the gauge section after cryogenic cyclic testing. Cross-sectional samples were extracted approximately

10 mm away from the delaminated region and then polished for SEM observation. This sampling location was selected to capture the local damage morphology associated with cryogenic cyclic failure while avoiding excessive disturbance from the fully separated fracture zone.

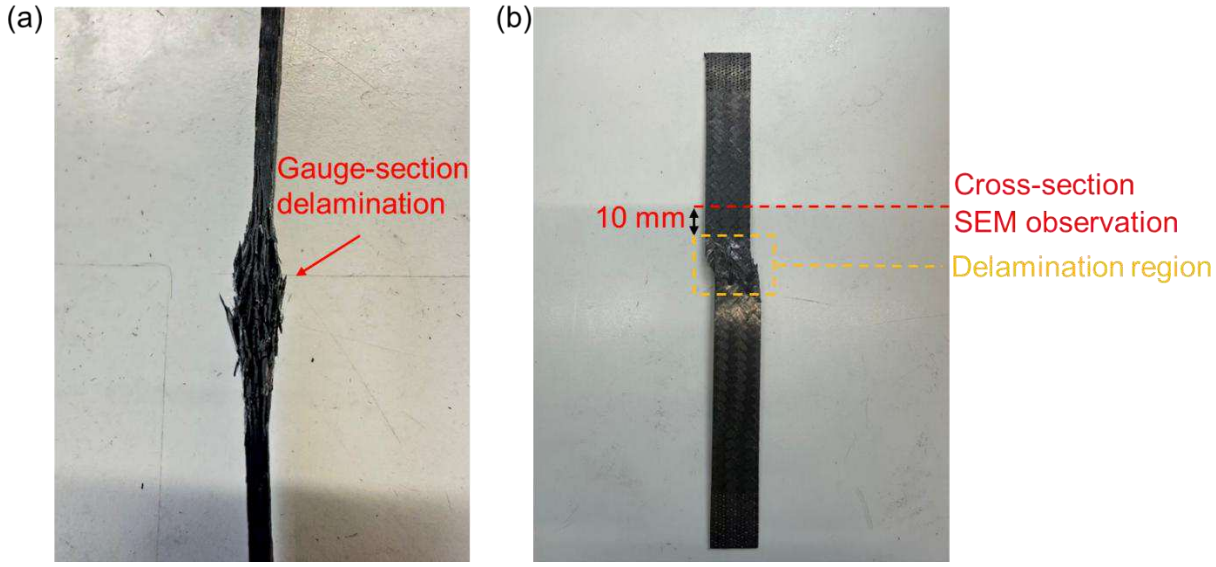


Figure 10. Macroscopic failure morphology and SEM sampling location after cryogenic cyclic tensile testing. (a) Delamination developed within the gauge section of the tensile specimen. (b) Cross-sectional SEM observation region selected approximately 10 mm away from the delaminated region.

Polished cross-sections from this region were then analysed by SEM shown in Figure 11. The pristine laminate exhibited extensive interlaminar damage, including pronounced delaminated regions and continuous interlaminar cracks (Figure 11a–c). At higher magnification, crack propagation along the interlaminar region was clearly observed, indicating that repeated cryogenic tensile loading promoted the formation and extension of matrix/interface-dominated damage. This extensive delamination is consistent with the premature failure of the pristine specimens during the cryogenic cyclic tests.

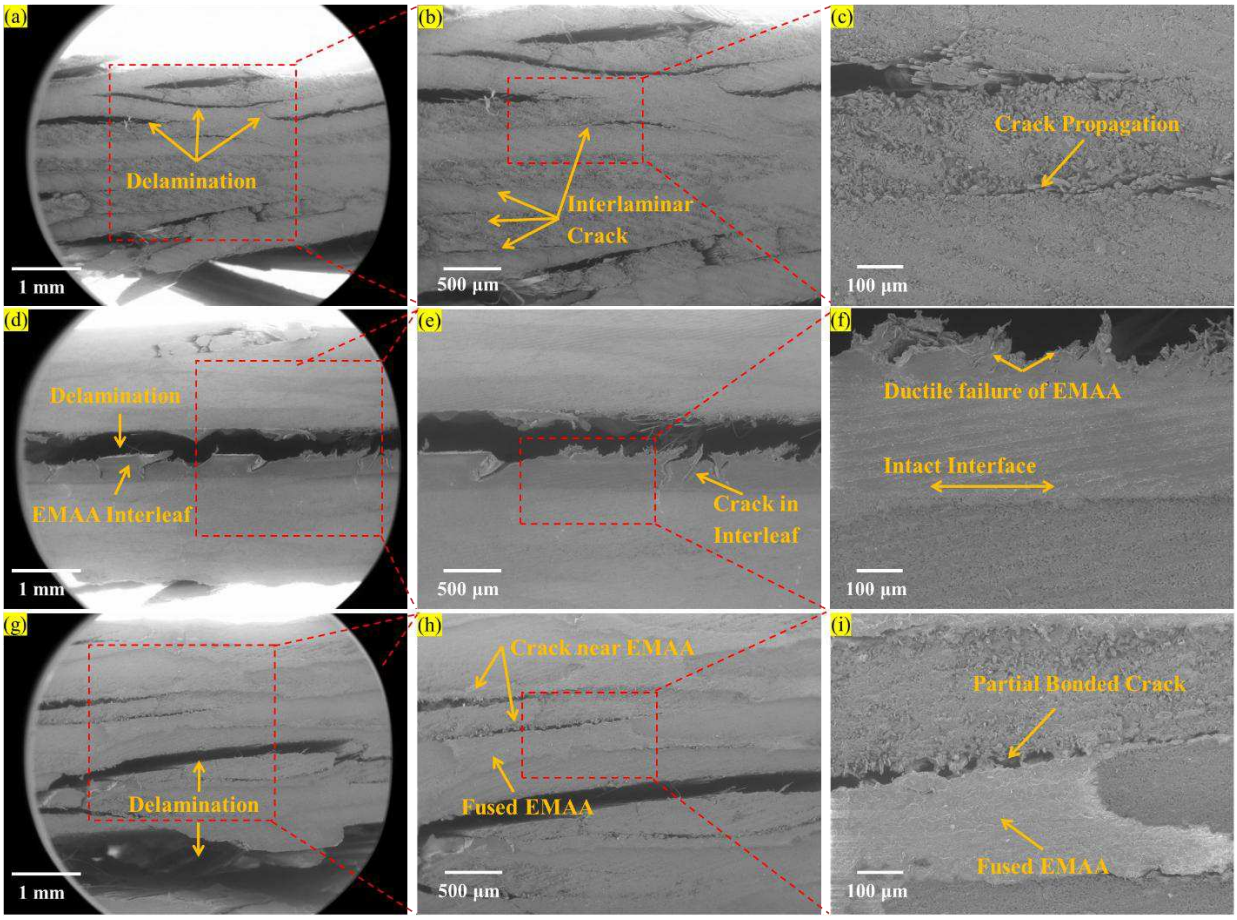


Figure 11. Post-cycling damage morphology near the fracture region after cyclic cryogenic tensile testing. (a–c) Pristine laminate, (d–f) interleaved self-healing (ISH) laminate, and (g–i) spray-coated self-healing (SSH) laminate. Red dashed boxes indicate the magnified regions shown in the adjacent panels.

In contrast, the ISH laminate showed damage concentrated around the EMAA interleaf region (Figure 11d–f). Although delamination was still observed along the interleaf, the high-magnification image revealed ductile deformation and tearing features within the EMAA phase, together with an intact interface adjacent to the interleaf. These features suggest that the EMAA interleaf functioned as a continuous damage-accommodation and healing zone during repeated thermal activation. The ability of the interleaf to undergo ductile deformation and maintain partial interfacial continuity is consistent with the superior residual cryogenic tensile performance of ISH, including its highest apparent residual strength and failure strain after repeated healing cycles.

For the SSH laminate, damage was more distributed through the laminate thickness (Figure 11g–i). Fused EMAA regions were observed near crack paths, indicating that the spray-coated EMAA particles melted and coalesced during thermal healing. In some regions, partially bonded cracks were visible, suggesting that the distributed EMAA phase contributed to local crack bridging or partial crack closure. However, residual cracks near EMAA-rich regions and incomplete bonding were also observed, which may explain why SSH retained high residual strength but did not reach the same recovery level as ISH. Compared with the continuous interleaf in ISH, the particulate and spatially distributed EMAA morphology in SSH appears less effective in restoring interlaminar continuity along dominant crack paths.

It should be noted that the present study focuses on tensile damage tolerance and mechanical recovery under liquid-nitrogen conditions, and direct measurements of gas permeability or leak-rate evolution were not performed. Nevertheless, the macroscopic observations and SEM analysis provide preliminary insights into the potential barrier-performance implications of the healing architectures. In particular, the ISH laminate exhibited limited crack propagation and reduced interlaminar damage after cryogenic cyclic loading, while evidence of EMAA redistribution was observed following thermal healing. The absence of extensive interconnected cracking suggests a reduced likelihood of forming continuous permeation pathways through the laminate thickness. Although these observations do not directly demonstrate permeability recovery, they indicate that the interleaving architecture may have the potential to restore barrier integrity after damage. Direct permeability and leak-rate measurements will be required in future work to establish the relationship between mechanical recovery, damage morphology, and hydrogen-barrier performance in linerless storage structures.

5. Concluding remarks

This study compared mid-plane interleaving and fibre-surface spray-coating as two routes for incorporating an EMAA thermoplastic healing phase into carbon-fibre/epoxy laminates for cryogenic hydrogen-storage applications. Although both approaches introduced comparable

EMAA contents, they produced distinctly different morphologies: ISH had a continuous mid-plane interleaf, whereas SSH had a distributed particulate architecture on fibre surfaces.

Under monotonic tensile loading at RT, the incorporation of EMAA reduced the initial stiffness and strength relative to the pristine specimen. At cryogenic temperature, however, all specimens became stiffer and less deformable, while the self-healing specimens exhibited larger modulus increases than the pristine specimen. Specifically, SSH reached a cryogenic tensile strength of 166.3 MPa, matching the pristine specimen (166.5 MPa), indicating that the spray-coated architecture was effective in preserving the initial cryogenic load-bearing capacity.

During cyclic loading, both self-healing architectures reduced stiffness degradation relative to the pristine specimen. At RT, ISH retained 88.3% of its initial modulus by the final cycle, compared with only 51.1% for the pristine specimen, whereas SSH retained 70.7%. Under cryogenic cyclic loading, both self-healing specimens completed the prescribed damage-healing cycles, while the pristine specimen failed prematurely. In the final cryogenic loading cycle, ISH exhibited the highest apparent residual strength, reaching 171.2 ± 2.4 MPa (112.7% of its monotonic cryogenic strength), while SSH retained 152.9 ± 5.1 MPa (91.9%). In addition, both self-healing specimens showed markedly greater deformation capacity than the pristine specimen, with the total tensile strain at final failure increasing from 3.3 ± 0.5% for the pristine specimen to 8.2 ± 0.1% for ISH and 7.2 ± 0.4% for SSH, corresponding to relative improvements of approximately 149% and 118%, respectively, compared with the pristine specimen.

Overall, the results demonstrate that the structural form and location of the healing phase strongly govern the mechanical response of self-healing CFRP samples under cryogenic loading. While both integration routes improved cyclic damage tolerance, mid-plane interleaving provided the most effective overall performance, particularly in terms of cyclic stiffness retention, residual cryogenic tensile strength, and final deformation capacity. SEM and macroscopic observations further revealed that the interleaved architecture suppressed extensive interlaminar crack propagation and delamination after cryogenic cyclic loading, whereas more pronounced damage

was observed in the pristine laminates. The observed reduction in interconnected damage pathways, together with evidence of EMAA redistribution during healing, suggests that the interleaving approach may also contribute to the recovery of barrier integrity by limiting the formation of through-thickness leakage paths. Although direct permeability measurements were beyond the scope of this study, these findings identify thermoplastic interleaving as a promising strategy for improving the cryogenic damage tolerance and residual mechanical performance of self-healing composite laminates, and potentially hydrogen-barrier functionality in self-healing composite laminates. The results provide useful guidance for the development of linerless Type V cryogenic hydrogen-storage structures.

Acknowledgment

The authors acknowledge the support of the HyPStore project and thank the Graphene Innovation Manchester team for their technical assistance and valuable contributions to this work.

Funding

This work was funded by Innovate UK under the HyPStore project (Grant No. 10112900).

Author contributions:

Conceptualization: Y.H. and T.L. Data curation: Y.H, L.W and H.C. Formal analysis: Y.H and T.L. Funding acquisition: L.B and T.L. Investigation: Y.H and T.L. Methodology: Y.H and L.W. Project administration: L.B and T.L. Resources: L.B and T.L. Software: Y.H. Supervision: T.L. Validation: Y.H. Visualization: Y.H. Writing—original draft: Y.H. Writing—review and editing: Y.H, L.B., and T.L.

References

[1] Züttel A. Hydrogen storage methods. Naturwissenschaften 2004;91:157–72.

[2] Hegde S, Shenoy BS, Chethan KN. Review on carbon fiber reinforced polymer (CFRP) and their mechanical performance. Mater Today Proc 2019;19:658–62.

[3] Usman MR. Hydrogen storage methods: Review and current status. Renewable and Sustainable Energy Reviews 2022;167:112743.

[4] Rivard E, Trudeau M, Zaghib K. Hydrogen storage for mobility: a review. Materials 2019;12:1973.

[5] Timmerman JF, Tillman MS, Hayes BS, Seferis JC. Matrix and fiber influences on the cryogenic microcracking of carbon fiber/epoxy composites. Compos Part A Appl Sci Manuf 2002;33:323–9. https://doi.org/10.1016/S1359-835X(01)00126-9.

[6] Islam MS, Chang W, Sha Z, Wang J, Wu S, Rose LRF, et al. Mitigating cryogenic microcracking in carbon-fibre reinforced polymer composites using negative thermal-expansion nanoparticles functionalized by a polydopamine coating. Compos B Eng 2023;257:110676. https://doi.org/10.1016/j.compositesb.2023.110676.

[7] Su Y fan, Zhang T yu, Sun H, Ma L hua, Zhou W. Cryogenic damage behavior of carbon fiber reinforced polymer composite laminates via fiber-optic acoustic emission. Compos Part A Appl Sci Manuf 2024;186:108435. https://doi.org/10.1016/j.compositesa.2024.108435.

[8] Griffith JC, Wang S, Palubiski DR, Ramakrishnan KR, Rochat S, Giuliani F, et al. Investigating the microcracking behaviour of a commercial epoxy matrix under cryogenic conditions. Compos Part A Appl Sci Manuf 2025;199:109190. https://doi.org/10.1016/j.compositesa.2025.109190.

[9] Grogan DM, Leen SB, Semprimoschnig COA, Ó Brádaigh CM. Damage characterisation of cryogenically cycled carbon fibre/PEEK laminates. Compos Part A Appl Sci Manuf 2014;66:237–50. https://doi.org/10.1016/j.compositesa.2014.08.007.

[10] Grogan DM, Ó Brádaigh CM, McGarry JP, Leen SB. Damage and permeability in tape-laid thermoplastic composite cryogenic tanks. Compos Part A Appl Sci Manuf 2015;78:390–402. https://doi.org/10.1016/j.compositesa.2015.08.037.

[11] Meng J, Zheng H, Wei Y, Liu D, Shi H, Wang P, et al. Leakage performance of CFRP laminate under cryogenic temperature: Experimental and simulation study.

Compos Sci Technol 2022;226:109550. https://doi.org/10.1016/j.compscitech.2022.109550.

[12] Yokozeki T, Ogasawara T, Aoki T, Ishikawa T. Experimental evaluation of gas permeability through damaged composite laminates for cryogenic tank. Compos Sci Technol 2009;69:1334–40. https://doi.org/10.1016/j.compscitech.2008.05.019.

[13] Meng J, Wang Y, Yang H, Wang P, Lei Q, Shi H, et al. Mechanical properties and internal microdefects evolution of carbon fiber reinforced polymer composites: Cryogenic temperature and thermocycling effects. Compos Sci Technol 2020;191:108083. https://doi.org/10.1016/j.compscitech.2020.108083.

[14] Hohe J, Schober M, Fliegener S, Weiss KP, Appel S. Effect of cryogenic environments on failure of carbon fiber reinforced composites. Compos Sci Technol 2021;212:108850. https://doi.org/10.1016/j.compscitech.2021.108850.

[15] Dry C. Procedures developed for self-repair of polymer matrix composite materials. Compos Struct 1996;35:263–9. https://doi.org/10.1016/0263-8223(96)00033-5.

[16] White SR, Sottos NR, Geubelle PH, Moore JS, Kessler MR, Sriram SR, et al. Autonomic healing of polymer composites. Nature 2001;409:794–7.

[17] Lee Hia I, Chan ES, Chai SP, Pasbakhsh P. A novel repeated self-healing epoxy composite with alginate multicore microcapsules. J Mater Chem A Mater 2018;6:8470–8. https://doi.org/10.1039/c8ta01783b.

[18] Pang JWC, Bond IP. A hollow fibre reinforced polymer composite encompassing self-healing and enhanced damage visibility. Compos Sci Technol 2005;65:1791–9. https://doi.org/10.1016/j.compscitech.2005.03.008.

[19] Trask RS, Bond IP. Biomimetic self-healing of advanced composite structures using hollow glass fibres. Smart Mater Struct 2006;15:704–10.

[20] Toohey KS, Sottos NR, Lewis JA, Moore JS, White SR. Self-healing materials with microvascular networks. Nat Mater 2007;6:581–5.

[21] Chen X, Dam MA, Ono K, Mal A, Shen H, Nutt SR, et al. A thermally re-mendable cross-linked polymeric material. Science (1979) 2002;295:1698–702.

[22] Cordier P, Tournilhac F, Soulié-Ziakovic C, Leibler L. Self-healing and thermoreversible rubber from supramolecular assembly. Nature 2008;451:977–80.

[23] Hager MD, Greil P, Leyens C, Van Der Zwaag S, Schubert US. Self-healing materials. Advanced Materials 2010;22:5424–30.

[24] Jony B, Thapa M, Mulani SB, Roy S. Repeatable self-healing of thermosetting fiber reinforced polymer composites with thermoplastic healant. Smart Mater Struct 2019;28:25037.

[25] Pingkarawat K, Wang CH, Varley RJ, Mouritz AP. Mechanical properties of mendable composites containing self-healing thermoplastic agents. Compos Part A Appl Sci Manuf 2014;65:10–8. https://doi.org/10.1016/j.compositesa.2014.05.015.

[26] Thorn TDS, Liu Y, Yao X, Papageorgiou DG, Robinson P, Bilotti E, et al. Smart and repeatable easy-repairing and self-sensing composites with enhanced mechanical performance for extended components life. Compos Part A Appl Sci Manuf 2023;165:107337. https://doi.org/10.1016/j.compositesa.2022.107337.

[27] Thorn TDS, Wang Y, Guo H, Lu L, Liu Y, Bilotti E, et al. Discontinuous interleaving strategies for toughening, damage sensing and repair in multifunctional carbon fibre/epoxy composites. Compos Part A Appl Sci Manuf 2024;185:108320. https://doi.org/10.1016/j.compositesa.2024.108320.

[28] Simonini L, Mahmood H, Dorigato A, Pegoretti A. Evaluation of self-healing capability of a polycaprolactone interphase in epoxy/glass composites. Compos Part A Appl Sci Manuf 2023;169. https://doi.org/10.1016/j.compositesa.2023.107539.

[29] Magyar B, Czigány T, Török D, Marton GZ, Balogh F, Szebényi G. Modeling of the Healing Process of Polycaprolactone-Interleaved Carbon Fiber–Reinforced Composites. Polym Compos 2025;46:14422–32.

[30] Wang CH, Sidhu K, Yang T, Zhang J, Shanks R. Interlayer self-healing and toughening of carbon fibre/epoxy composites using copolymer films. Compos Part A Appl Sci Manuf 2012;43:512–8. https://doi.org/10.1016/j.compositesa.2011.11.020.

[31] Pingkarawat K, Wang CH, Varley RJ, Mouritz AP. Self-healing of delamination fatigue cracks in carbon fibre–epoxy laminate using mendable thermoplastic. J Mater Sci 2012;47:4449–56.

[32] Peñas-Caballero M, Chemello E, Grande AM, Hernández Santana M, Verdejo R, Lopez-Manchado MA. Poly(ethylene-co-methacrylic acid) coated carbon fiber for self-healing composites. Compos Part A Appl Sci Manuf 2023;169. https://doi.org/10.1016/j.compositesa.2023.107537.

[33] Laban O, Pearce G, Zhang J, Islam MS, Djukic LP. A comparative study of the cryogenic performance of CFRP composites with polyethersulfone/epoxy blends and electrospun polyethersulfone interleaves. Compos Part A Appl Sci Manuf 2024;178:108000. https://doi.org/10.1016/j.compositesa.2023.108000.

[34] Grenoble R, Gates T. Hydrogen permeability of polymer matrix composites at cryogenic temperatures. 46th AIAA/ASME/ASCE/AHS/ASC structures, structural dynamics and materials conference, 2005, p. 2086.

[35] Lei L, Yan Y, Liu T, Hao Y, Chai J, Zhuang Z, et al. Permeability modeling and mechanical performance of multi-ply heterogeneous composites for linerless hydrogen storage tanks. Composites Part B 2026;322:113743. https://doi.org/10.1016/j.compositesb.2026.113743.

[36] Advani SG, Hsiao K-T. Manufacturing techniques for polymer matrix composites (PMCs). Elsevier; 2012.

[37] Long AC. Design and manufacture of textile composites. Elsevier; 2005.

[38] Astm 3039. D 3039/D 3039M Standard Test Method for Tensile Properties of Polymer Matrix Composite Materials 1. n.d.

[39] Schneider CA, Rasband WS, Eliceiri KW. NIH Image to ImageJ: 25 years of image analysis. Nat Methods 2012;9:671–5.

[40] Marino SG, Czél G. Development and characterisation of reparable, film-interleaved, pseudo-ductile hybrid composites. Compos Part A Appl Sci Manuf 2023;169:107496. https://doi.org/10.1016/J.COMPOSITESA.2023.107496.

[41] Magyar B, Czigany T, Szebényi G. Metal-alike polymer composites: The effect of inter-layer content on the pseudo-ductile behaviour of carbon fibre/epoxy resin materials. Compos Sci Technol 2021;215:109002. https://doi.org/10.1016/J.COMPSCITECH.2021.109002.